DEVCOM
ARMY RESEARCH
LABORATORY

Methods for Microstructure Modeling and Phase Field Simulations of Fracture

by R Brian Leavy, John D Clayton, Jonathan P Ligda, and Jaroslaw Knap

NOTICES

Disclaimers

The findings in this report are not to be construed as an official Department of the Army position unless so designated by other authorized documents.

Citation of manufacturer's or trade names does not constitute an official endorsement or approval of the use thereof.

Destroy this report when it is no longer needed. Do not return it to the originator.

DEVCOM
*ARMY RESEARCH
LABORATORY*

Methods for Microstructure Modeling and Phase Field Simulations of Fracture

R Brian Leavy, John D Clayton, Jonathan P Ligda, and Jaroslaw Knap
Army Research Directorate, DEVCOM Army Research Laboratory

REPORT DOCUMENTATION PAGE

1. REPORT DATE *(DD-MM-YYYY)*	2. REPORT TYPE	3. DATES COVERED (From - To)
June 2023	Technical Report	October 2020–March 2023

4. TITLE AND SUBTITLE	5a. CONTRACT NUMBER
Methods for Microstructure Modeling and Phase Field Simulations of Fracture	
	5b. GRANT NUMBER
	5c. PROGRAM ELEMENT NUMBER
6. AUTHOR(S)	**5d. PROJECT NUMBER**
R Brian Leavy, John D Clayton, Jonathan P Ligda, and Jaroslaw Knap	
	5e. TASK NUMBER
	5f. WORK UNIT NUMBER

7. PERFORMING ORGANIZATION NAME(S) AND ADDRESS(ES)	8. PERFORMING ORGANIZATION REPORT NUMBER
DEVCOM Army Research Laboratory ATTN: FCDD-RLA-TF Aberdeen Proving Ground, MD 21005-5066	ARL-TR-9703

9. SPONSORING/MONITORING AGENCY NAME(S) AND ADDRESS(ES)	10. SPONSOR/MONITOR'S ACRONYM(S)
	11. SPONSOR/MONITOR'S REPORT NUMBER(S)

12. DISTRIBUTION/AVAILABILITY STATEMENT
Approved for public release; distribution is unlimited.

14. ABSTRACT
Tools for modeling fracture and other structural transformation processes in polycrystalline materials are developed. Methods for construction of 3-D realizations of polycrystalline microstructures using experimental characterization data are described. Underlying statistics are discussed, and a workflow from statistical descriptors of microstructure to geometric rendering to finite element (FE) meshes is demonstrated. A formulation of the phase field method (PFM) with order parameter kinetics for transient processes is presented. This formulation is implemented in FE software with a unique implicit integration of the phase field kinetic equation. Simulations of fracture of ceramic polycrystals demonstrate the utility of the tools developed for synthetic microstructure generation and the effectiveness of the implicit dynamic implementation of the PFM. Results quantify effects of variations of initial microstructure features on dynamic tensile strength of polycrystals. Larger tensile strengths predicted by simulations relative to experiments are reconciled by Weibull scaling.

15. SUBJECT TERMS

microstructures, ceramics, polycrystals, fracture mechanics, phase field

16. SECURITY CLASSIFICATION OF:			17. LIMITATION OF ABSTRACT	18. NUMBER OF PAGES	19a. NAME OF RESPONSIBLE PERSON R Brian Leavy
a. REPORT Unclassified	**b. ABSTRACT** Unclassified	**c. THIS PAGE** Unclassified	UU	54	**19b. TELEPHONE NUMBER (Include area code)** 410-278-7982

Contents

List of Figures

List of Tables

iv

Acknowledgments

1. Introduction

Many, if not most, strong structural engineering materials are polycrystalline. Examples include metals and their alloys, ceramics, stone, and concrete, the latter being a mixture of crystalline materials of geologic origin. Understanding how features of polycrystalline microstructures, including physical properties and geometries of constituent grains, affect the overall response of these materials is a goal of contemporary theoretical and computational modeling. Tools developed in recent years for simulating the mechanical response, encompassing elasticity, inelasticity, and fracture, of polycrystalline materials are described in the present report.

Elasticity theory is well established for crystalline materials. Classical linear elasticity as well as nonlinear elasticity based on the traditional Green-Lagrangian strain are described in the literature, for both isotropic solids and for anisotropic crystals.[1–3] Depending on the loading conditions, other finite strain measures (e.g., Eulerian, logarithmic, or those obtained from a QR decomposition) have been shown to be more effective in analytical research published over the past decade.[4–8] Parameters (e.g., second- and higher-order elastic constants as well as thermal expansion coefficients) can be measured using standard experimental techniques, and these parameters have a sound physical basis at the scale of atomic bonding, vibrations, and lattice structure.[3,9]

Many different models for inelasticity and fracture exist, and none are universally accepted. Classical models for macroscopic[10] and single crystal[11,12] plasticity, being devoid of an intrinsic length scale, are unable to capture size effects and can suffer from unrealistic mesh dependency of solutions in numerical implementations. Popular models for dynamic plasticity[13] also rely on physically unwieldy parameters that may be difficult to assign uniquely given a set of experimental data. Such calibrated parameters lack correlation with physical mechanisms at the scale of atoms or discrete defects such as dislocation lines. Similar deficiencies apply to phenomenological models for phase transitions, twinning, and damage mechanics.[14–16] Calibration of parameters is cumbersome and not always physically justified, and no regularization length is incorporated.

Numerical simulations of fracture in crystalline microstructures were advanced in the 1990s and early 2000s with the advent of the cohesive zone finite element method (CZFEM). This technique has been applied to inclusion debonding in a sin-

gle crystal matrix,[17] polycrystal plasticity with grain boundary fracture,[18,19] and dynamic fracture in biologically inspired systems[20] and impacted ceramics.[21] Promising results were achieved in these applications, but the method can suffer from crack-path dependency of the FE mesh construction. Numerical implementations of CZFEM are computationally costly since changes in topology must be resolved explicitly, and since contact algorithms must be used to prevent interpenetration of newly created surfaces for compressive states. Parameters can be assigned based on interatomic potentials,[17] but more often, cohesive behavior is calibrated to macroscopic strength. The material point method (MPM) is another contemporary technique that has been successfully applied toward modeling of polycrystal mechanics; Leavy et al.[22] report further details.

The phase field method (PFM) has emerged over the past two decades as one of the most robust and physically realistic approaches to modeling structural transformations in solids, including fracture. The theory contains a regularization length that mitigates improper mesh dependence in numerical simulations. Mesh topology is preserved, facilitating computational efficiency, notably in parallel computing environments. Furthermore, the number of parameters required is minimal. Such parameters can usually be assigned a clear physical significance and can often be obtained from conventional experimental data or atomic-scale properties. Pioneering work[23] employed a variational approach with incremental energy minimization to update the order parameter and linear isotropic elasticity, locally degraded by fracture, to describe the stress-strain response. In addition to the two elastic constants, only two parameters are needed to model isotropic fracture: the surface energy and the regularization length. The former can be obtained from atomic simulations or experimental measurements of fracture toughness. The latter can be assigned based on mesh size limitations, or it can be derived from knowledge of the surface energy and the tensile strength.[24]

Subsequent fundamental research on the PFM for fracture mechanics by the present co-authors is summarized briefly. Novel theories considered nonlinear elasticity[25] and anisotropic elasticity with anisotropic cleavage energy.[26] Coupling of fracture with deformation twinning,[27] solid-solid phase transformations,[28,29] and crystal plasticity[29,30] has also been studied using phase field methods. Phase field theories and corresponding numerical simulations for twinning[31–33] were developed prior to those coupled with fracture.

2

Around the same time, other researchers studied martensitic phase transformations[34] and coupled slip-twinning phenomena[35] with the PFM. Extensions such as use of a phase field to represent ductile fracture in an otherwise elastic-plastic continuum have become widespread.[36,37]

Enriched theories for structural transformations in nonlinear materials incorporating concepts and tools of Finsler geometry were set forth in 2016,[38–40] whereby connections with PFM, micropolar, micromorphic,[41] and other gradient-based models were demonstrated. Use of a Riemannian rather than Finslerian metric enabled reduction of the equilibrium equations derived for certain classes of energy potentials of the Finsler geometric theory[39,42] to those of the PFM. Such differential geometric models, like their phase field counterparts, have been investigated through analytical solutions[42] and numerical simulations[28,43,44] of fracture and phase transformations.

More recent theory for the PFM, with consistent thermodynamics and proper resolution of finite strains and rotations, accounts for stress-state influences on material strength, very large pressures, adiabatic heating, residual stress, and dissipation of viscous origin.[45–47] Structures of high-pressure shock waveforms in polycrystals were recently resolved using phase field methods in one-dimensional (1-D) simulations.[48] Heterogeneous grain and phase boundary properties have been recently implemented in 3-D phase field simulations of fracture of ceramic composites.[49–51]

The current report is focused on application of the PFM for fracture, twinning, and other structural transformations to three-dimensional (3-D) simulations of deforming polycrystals. Two very recent works[52,53] implemented dissipative kinetics for fracture in 3-D simulations of polycrystalline microstructures, specifically ceramics consisting of anisotropic grains of boron carbide (B_4C) or titanium diboride (TiB_2). Underlying tools used to produce numerical results reported in those works,[52,53] as well as demonstrative new computational results, are described in this report. The computational methods described herein thus supplement the constitutive theory, results, and their interpretations published elsewhere; for example, the present content was too large to be included in a prior work of restricted length.[53]

Section 2 describes methods for 3-D microstructure rendering and FE mesh generation, including statistical descriptors and protocols for linking several third-party software packages. Section 3 describes the underlying theory and solution methodologies for static and dynamic PFM implementations in current FE software; the

original source code was written at the US Army Combat Capabilities Development Command (DEVCOM) Army Research Laboratory (ARL) at Aberdeen Proving Ground, Maryland, over a decade ago.[33] This code has been continually upgraded to accommodate broader physics and more efficient, larger-scale computations on evolving parallel platforms. Section 4 presents previously unpublished results from PFM on fracture in anisotropic polycrystalline ceramics, newly quantifying effects of different microstructure realizations and orientations based on the same experimental statistics.

2. Microstructure Modeling

Materials of current interest[30,54] are polycrystalline B_4C, polycrystalline TiB_2, and a B_4C-TiB_2 composite consisting of an average volume fraction of 23% TiB_2.

2.1 Characterization

An image of the microstructure for the B_4C-23 vol.%TiB_2 material[54] produced by spark plasma sintering (SPS) with fine TiB_2 particles is shown in Fig. 1. This image is obtained from scanning electron microscopy (SEM).
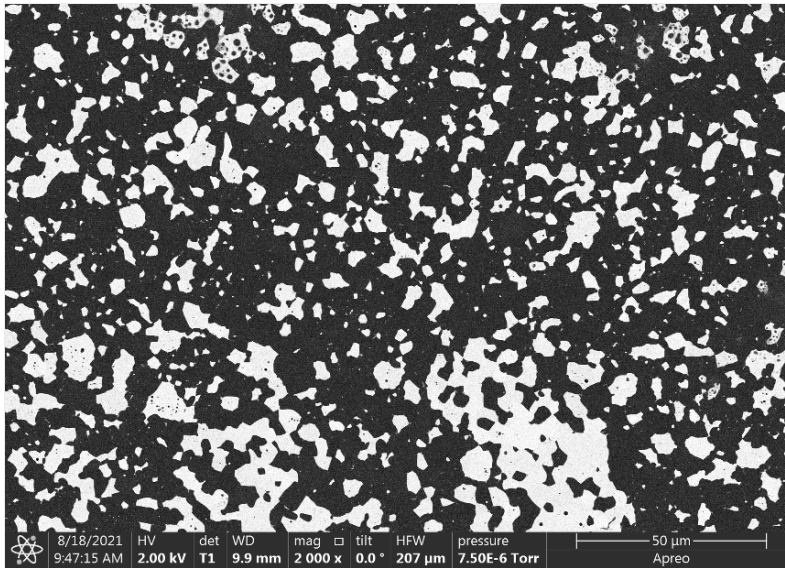
Fig. 1 SEM image of experimental microstructure for a B_4C-TiB_2 composite material, showing the composition of B_4C (dark) and TiB_2 (light)

Scans from electron backscatter diffraction (EBSD), as shown in Fig. 2 for composites of B_4C-23 vol.%TiB_2 with fine and coarse TiB_2 particles, provide lattice orientation information for crystalline phases and further insight on grain size dis-

tributions, supplementing data extracted from SEM.

(a) Fine-grained material (45 μm scale)

(b) Coarse-grained material (100 μm scale)
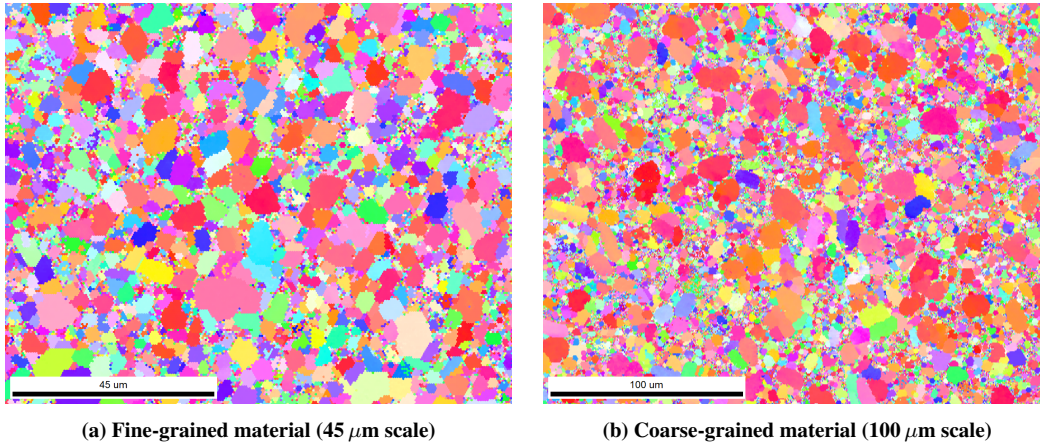
Fig. 2 EBSD images of experimental microstructures for B$_4$C-TiB$_2$ composite materials

The individual materials are shown separately for the coarse grain material in Fig. 3. The size difference between the smaller B$_4$C and the larger TiB$_2$ grain diameters is noted using the same 100 μm scale.

(a) Boron carbide grains

(b) Titanium diboride grains
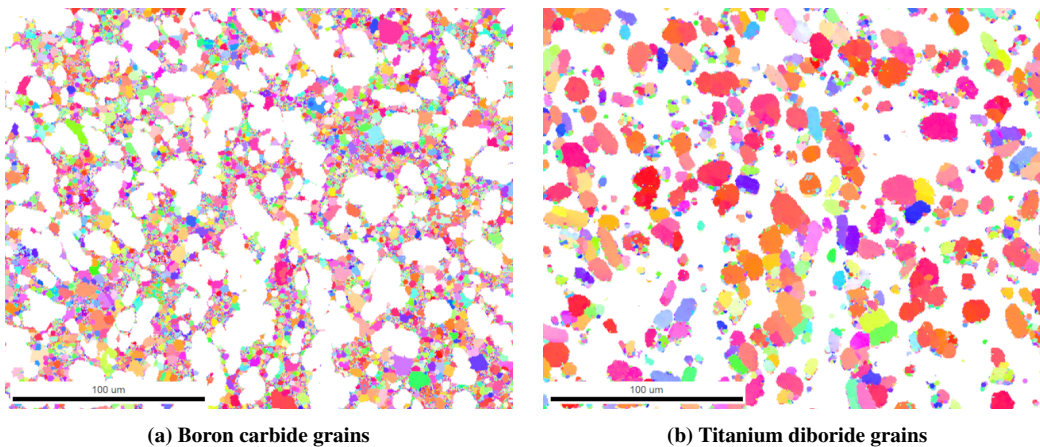
Fig. 3 EBSD images of the coarse-grained composite separated by material

From micrographs and scans such as these, area fractions and size distributions of separate materials can be quantified. For example, grain size distributions of phases are reported by Rubink et al.[54] for this material system. Statistical analysis using a single slice of EBSD data from the authors will be discussed in the next section. Simulations and analysis are all based on the coarse grain B$_4$C-23 vol.%TiB$_2$ material.

5

2.2 Statistics

Ideally, full 3-D microstructures are reconstructed from either destructive 3-D EBSD or non-destructive high energy X-ray diffraction microscopy (HEDM). With regard to HEDM, it is currently unclear how successful 3-D volumes of these multiple phases can be determined using HEDM reconstruction. For the current analysis, the 2-D EBSD grain areas from a coarse grain B_4C-TiB_2 slice are extracted using image analysis software.[55] A single EBSD slice may sample smaller 2-D grain diameters if the 3-D volume of a grain is not sliced at the equator when calculating an average grain diameter.

In Fiji,[55] the EBSD images are modified to use average color to improve the determination of grains with varied IPF color orientations. Next, the length scale of the image are set to equate pixels to microns. For our images, this equated to 4.84 pixels per micron. Then, area measurements are created using an Analyze Particles filter.

The resultant grain area information was saved and then analyzed using a Jupyter Python notebook.[56,57] The experimental data were fit for the grain size equivalent diameters using a lognormal probability density function (PDF). The individual material phases were fit separately for the B_4C grains and the TiB_2 grains, and the resultant statistics used to generate synthetic representations of the ceramic microstructure, as discussed in Section 2.3.

Statistics for the B_4C grains in the composite material are illustrated by the PDF distribution and fit in Fig. 4a.

(a) PDF for B_4C grains   (b) PDF for TiB_2 grains
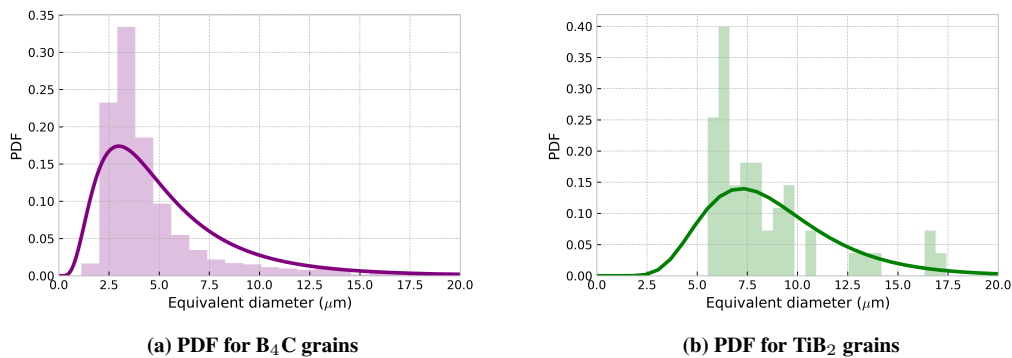
Fig. 4 PDFs for individual material phases

Statistics for the B_4C grains in the composite material are illustrated by the PDF distribution and fit in Fig. 4a. The experimental statistics and fit for the TiB_2 material in the composite is shown in Fig. 4b. In this data set, the TiB_2 grains are larger on average than the B_4C grains. Comparisons to a theoretical starting distribution of grain diameters can be assessed using Kolmogorov-Smirnov (KS) statistics.[58]

The Kolmogorov-Smirnov test compares a sample cumulative frequency with the continuous cumulative distribution function (CDF) of a theoretical distribution.[59] If the discrepancy between the theoretical and the sample is below a critical value, then it is considered acceptable for a given significance level α.

Given a sample of size N, the data are sorted in increasing order to create an estimated distribution (eCDF) or sample cumulative frequency $S_N(x)$,

$$
\begin{aligned}
S_N(x) &= 0 & x &< x_1 \\
&= \upsilon(k, N) & x_k &\leq x < x_{k+1} \\
&= 1 & x &\geq x_N,
\end{aligned}
\tag{1}
$$

where $x_1, x_2, ..., x_N$ are the ordered data of observed values. and $\upsilon(k, N)$ is an estimator function, typically defined as either*

$$
\upsilon(k, N) = \frac{k}{N} \qquad \text{or} \qquad \upsilon(k, N) = \frac{k - 1/2}{N}.
\tag{2}
$$

The values of k range from 1 to $N - 1$. For our example, the x_N correspond to the equivalent diameters of the individual grains, in microns.

The maximum difference between the estimated sample eCDF [i.e, $S_N(x)$] and the theoretical CDF [i.e., $F(x)$] over the entire range of x is a measure of the discrepancy. This discrepancy is the KS statistic:

$$
D_N = \max |F(x) - S_N(x)| = \max_i |F(x_i) - S_N(x_i)|,
\tag{3}
$$

where the discrete form follows from monotonicity of both the CDF and eCDF.

---

*When there is some knowledge of the expected nature of the source distribution, other estimator functions might be adopted to minimize the discrepancy between the CDF and eCDF, but the second form listed here seems to produce the best results when sample size is suboptimal.

Kolmogorov developed the asymptotic distribution for the discrepancy as

$$\pi(\Delta r, N) = \lim_{N \to \infty} P(D_N \leq \Delta r) = 1 - 2 \sum_{k=1}^{\infty} (-1)^{k-1} \exp\left(-2Nk^2 \Delta r^2\right). \quad (4)$$

By introducing a change of variables, $z = \sqrt{N} \Delta r$ so that $\pi(\Delta r, N) = \pi(z/\sqrt{N}) = p(z)$,

$$p(z) = \lim_{N \to \infty} P(D_N \leq \frac{z}{\sqrt{N}}) = 1 - 2 \sum_{k=1}^{\infty} (-1)^{k-1} \exp\left(-2k^2 z^2\right). \quad (5)$$

The result, $p(z)$, is the probability that the KS statistic D_N will be less than a certain value $z/\sqrt{N}$ for the given sample size N. This observed maximum difference L_∞ norm D_N is compared to a given critical value D_N^α. The significance level α is used to determine the confidence level $(1 - \alpha)$:

$$P(D_N \leq D_N^\alpha) = 1 - \alpha. \quad (6)$$

To determine how many grain diameters are required to have 95% confidence that the maximum error in the eCDF is smaller than 10%, set $\Delta r = 0.1$ and $P(D_N \leq 0.1) > 0.95$. This corresponds to the condition that $\pi(0.1, N) = 0.95$. Therefore, solving Eq. 4 for N then requires 184 diameters. This result corresponds to $z = 1.3581$.[60] The maximumum number of grains used in this study was 117. Accordingly, to explore different Δr values, the synthetic statistics tabulated in this section are determined from

$$d_\alpha = d_{0.05} = \frac{1.3581}{\sqrt{N}}. \quad (7)$$

For our specific example, the cumulative distribution function is

$$F(x) = \frac{1}{2} \text{erfc}(\frac{\mu - \log(x)}{\sqrt{2}\sigma}). \quad (8)$$

To generate synthetic realizations of grain diameters X, the inverse of the complementary error function for the CDF

$$X = F^{-1}(r) = e^{-\mu\sigma\sqrt{2}\,\text{erfc}^{-1}(2r)} \quad (9)$$

(a) CDF for B$_4$C grains   (b) CDF for TiB$_2$ grains
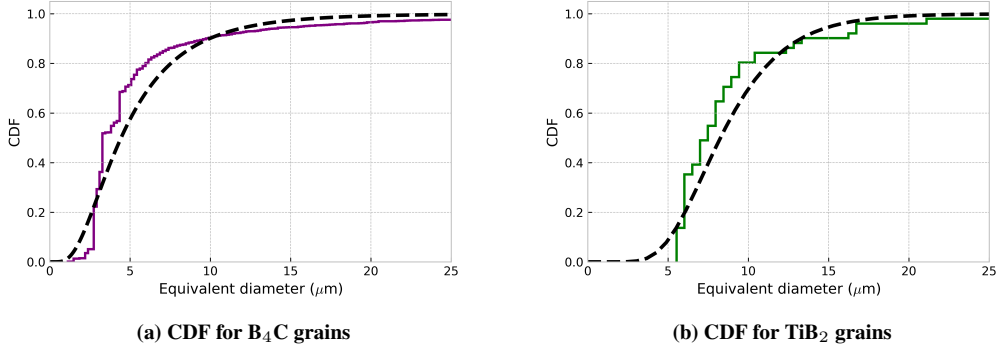
Fig. 5 CDFs for individual material phases

is used, with random numbers r generated in the range of zero to one. The probability density function, or the derivative of the differentiable CDF is

$$f(x) = \frac{1}{x\sqrt{2\pi}\sigma}e^{-\frac{(\log(x)-\mu)^2}{2\sigma^2}}, \tag{10}$$

with the mean μ, and standard deviation σ used for synthetic generation based on a fit to the experimental characterization data.

It was previously determined by Brannon et al.[61] that a numerical comparison with a large number of generated eCDFs is superior to the KS statistics, given the limited numbers of grains in most mesoscale simulations. The KS statistics results for our SVEs are summarized in Section 2.4.

The CDF for the B$_4$C grains is shown Fig. 5a. The B$_4$C CDF fit calculated a mean $\mu = 1.491$ and standard deviation $\sigma = 0.6292$. The majority of grain diameters fell in the $1 - 10$ micron range, with an average diameter of 6.27 micron.

The fit for the TiB$_2$ grains is shown in Fig. 5b. The TiB$_2$ CDF fit calculated a mean $\mu = 2.112$ and standard deviation $\sigma = 0.3698$. The majority of the TiB$_2$ EBSD grain diameters fell in the $5 - 30$ micron range, with an average diameter of 8.97 micron. For comparison, the 2-D SEM had a larger sampling of grains and calculated an average grain diameter for the TiB$_2$ grains of 14 micron.

If all the EBSD grains were used in one lognormal fit, the distribution would have a calculated mean $\mu = 2.305$ and standard deviation $\sigma = 0.4958$. The average grain diameter was 11.67 micron. Grains below approximately two microns are ignored

9

for the EBSD fit to all the grains, for better comparison to the synthetic generated microstructures generated with small grains removed.

The statistical results presented in this report are used for synthetic microstructure generation in the Digital Representation Environment for the Analysis of Microstructure in 3 Dimensions[62] (DREAM3D). The procedures for statistical characterization, synthetic generation, and smoothing follow the work of Leavy et al.[22]

2.3 Synthetic Generation

The software package DREAM3D is used to generate synthetic microstructures for the B_4C and TiB_2 based ceramics. Techniques have been developed to read X-ray high-energy diffraction microscopy (HEDM) data sets, which determine the individual grain geometries and orientations in multiple planes. The software combines the individual planes into a 3-D microstructure, attempting to connect and orient the individual grains properly with additional tools. Similar techniques using these tools have been demonstrated in the work of Spear.[63] The resulting microstructures can then be analyzed, and their statistical distributions can be exported. Similar techniques involving EBSD have been used previously.[64,65] Until HEDM volume data are available for the materials of present interest, the relevant statistics for characterization have been extracted from SEM and EBSD. From the microstruc-

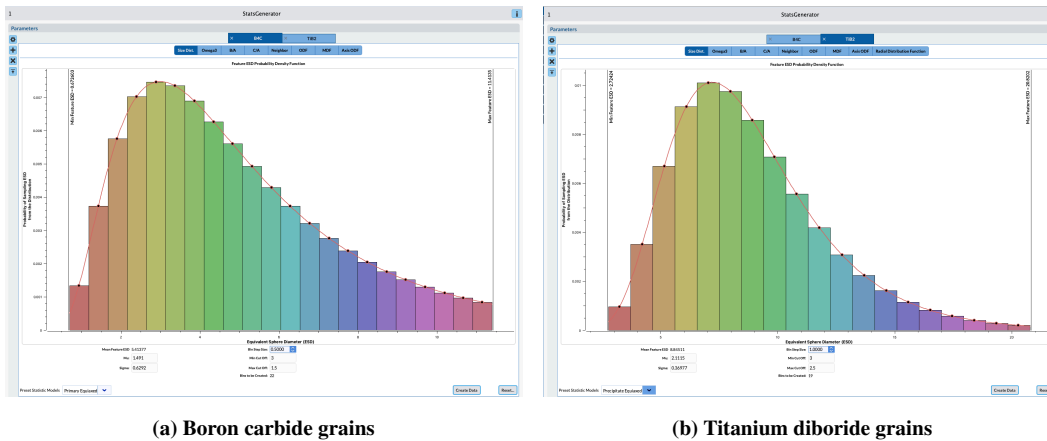(a) Boron carbide grains   (b) Titanium diboride grains

Fig. 6 Grain size distributions used in DREAM3D for synthetic microstructure generation

ture statistics, the DREAM3D statistical generator filter is used to create a synthetic microstructure. Previous work examined a diamond-silicon carbide ceramic composite,[49,50] while similar techniques are applied to the B_4C-TiB_2 system. An ex-

ample of the DREAM3D gui for the B_4C-TiB_2 composited material's two separate phases is shown in Fig. 6.

First the calculated percentage of individual material volume percents are input. Second, the crystal structure for the individual materials is input. Here, B_4C is rhombohedral (i.e., trigonal symmetry) and TiB_2 is hexagonal. Third, the grain size distributions calculated previously are input. The lognormal distributions are then truncated based on the range of equivalent diameters for the material.

Fourth, the materials are defined as either primary phases or precipitates. For our example, the TiB_2 material is defined as the precipitate phase. If the materials are defined to be precipitates, then a distance distribution between precipitates can be created. This procedure was used along with the volume fraction percent to get the TiB_2 grains dispersed throughout the B_4C primary phase.

Fifth, the shape type for the materials is defined. Ellipsoids as roughly spherical shapes were chosen for both grain materials. The TiB_2 grains may be more disc shaped in actuality, but these shape properties were not attempted in the following simulations. Then, if orientation information from actual microstructures is available, the orientation distributions can be input. Our current examples are created using random lattice orientation distributions, but textured distributions could be used if data collected from EBSD scans such as Fig. 2 warrants this. Subsequent analysis of our material suggests that the TiB_2 grains have a preferred [0001] texture (i.e., a basal texture or fiber texture) for the coarse-grained material.

Next, the DREAM3D filters for synthetic generation input the edge length, with a resolution or spacing used to determine how coarse the voxelized synthetic volume element (SVE) should be. Other filters then match the crystallography and export the voxelized mesh.

Fig. 7 shows the voxelized SVE 9 realization generated by DREAM3D, with tranparent B_4C grains colored by the inverse pole figure (IPF) orientation color. The dark gray grains are the TiB_2 grains.
The stair-stepped meshed description can be seen more clearly in the TiB_2 grains.
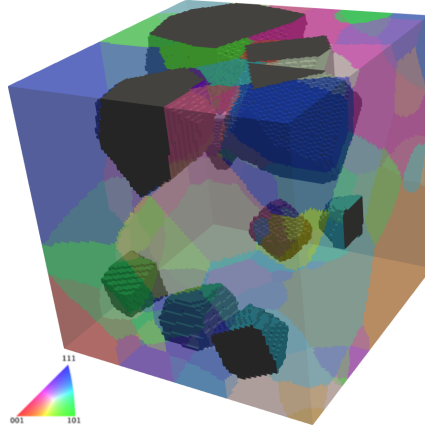
Fig. 7 Voxelized synthetic microstructure created from DREAM3D with B$_4$C grains colored by IPF and TiB$_2$ grains in gray

2.4　Conformal Meshing

Synthetically generated representative volume elements from DREAM3D are exported as Abaqus[66] files in a voxelized hexahedral format. A procedure was developed for converting the stair-stepped hexahedral description of grain geometries into conforming smooth hexahedral or tetrahedral domain descriptions. These FE meshes are then available for mechanics simulations using a phase field code.[33,52]

Steve Owen created a sculpting tool (Sculpt) for use with the meshing software Cubit[67] at Sandia National Laboratories, which can be utilized at the command line in a massively-parallel format for creating conforming hexahedral meshes.[68] Examples of the Sculpt tool for hexahedral SVE generation can be seen in the work of Lim et al.[69] Comparisons can be made between the standard voxelized geometry descriptions and conforming geometries.

In Fig. 8, the procedure that the Sculpt tool uses for creation of material fitted meshes is illustrated. From left to right in the figure, the first step is to create a Cartesian grid which overlays the geometry. From there, the nearby nodes are projected to the boundaries, as seen from the second image from the left. The third step shows the procedure by which the mesh pulls away from the boundaries. In step four, a layer of hexes is inserted. Finally, in the rightmost image, smoothing and other methods are performed to improve the element quality.
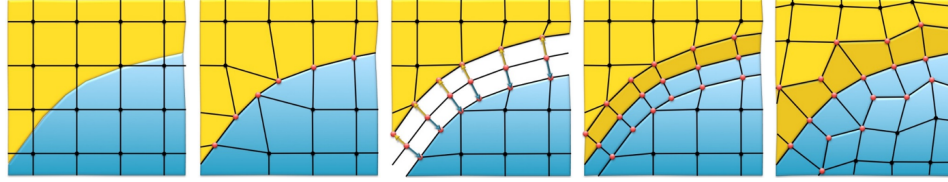
Fig. 8 Sculpt-based mesh refinement of boundaries[68]

The procedures of the present work utilize the latest versions of Cubit and Sculpt with some additional features for an improved surface description, including surface cleanup and the removal of small domains. A means to directly create tetrahedral meshes from the geometry created in Sculpt is being explored at Sandia National Laboratories, but this is not currently available.

Starting with a microstructure geometry and an orientation description from the DREAM3D tools in Abaqus format, the voxelized mesh is converted to Exodus[70] format. The voxelized hexahedral mesh is then used as the input for Sculpt. The original voxelized files can be exported as Exodus files for comparison to the improved smooth hexahedral or tetrahedral meshes thus created.

For smooth hexahedral descriptions, a combination of Laplacian/Optimization (Hybrid) surface and volume smoothing options is used. Results are best with the surface nodes not projected to the interpolated surface. Optional boundary buffer improvements are currently not being used. A Hermite interpolation for the curve smoothing worked best for the microstructures examined in this project. The chosen procedures are useful for smoothing noisy surfaces that are traditionally seen with stair-stepped input geometries, like the current starting voxelized microstructures. An optional defeature option is currently used, which filters and collapses objects below a critical volume, as well as protusions. Next, the conforming smooth hexahedral mesh is saved, for smooth hex grain simulations, if desired.

The current version of Sculpt is also able to generate a triangle mesh of the surface geometry. The surface geometry is based on the input grid resolution and the various smoothing options chosen in Sculpt. An Exodus file is exported with a file extension (*.s2g*), which contains additional geometry association information. The file is imported as a development option into Cubit using the command "*import s2g filename.s2g*".

Cubit can generate tetrahedral meshes using the *TetMeshGems* method. Such a mesh is then saved in Exodus format. Tetrahedral volume elements often better approximate the actual geometries, though most prior 3-D phase field studies[25,26,50,52,53] have used hexahedral elements. Full-integration hexahedral elements have been found to more accurately represent contours of the phase field than the same number of standard (i.e., one-point integration) tetrahedra. Other tools explored for grain boundary smoothing of hexahedral descriptions can be seen in the work of Maddali and Suter.[71] They developed some Matlab tools outside of DREAM3D for grain boundary smoothing.

The Exodus hexahedral or tetrahedral meshes are used as input to the phase field code. Adaptive element sizes, or a fixed size, may be chosen based on the application. This entire procedure has been automated at the command line, and used for generation of the simulated microstructures. An example synthetic generation and the resultant smooth meshes created for SVE 7 are shown in Fig. 9.

In this example, small features are removed and reshaped as the initial voxelized mesh from DREAM3D is smoothed and defeatured. In Fig. 9a, the small grains like the red one are removed, and pink objects are rounded in the smooth sculpted versions of the mesh. The smooth hexahedral meshes (e.g., Fig. 9b) are used for all the results in this report. The tetrahedral mesh option (e.g., Fig. 9c) is another phase field option that was not used for this series of simulations.

Methods for insertion of thin layers of material between crystals to account for distinct grain or phase boundary properties have been previously implemented, with positive outcomes. Smoothing of geometry followed by mesh refinement, in these layers and in their vicinity to enable better resolution of grain boundary fracture, has been successful. Details of phase field simulations incorporating such smoothed and refined meshes are discussed in several published works.[49,50]
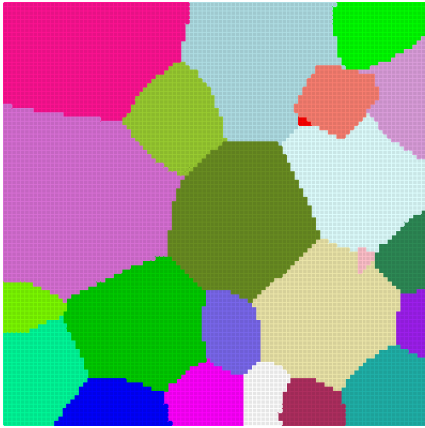
(a) Voxelized hexahedral mesh
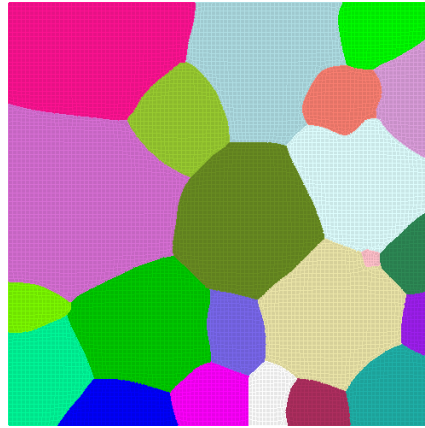
(b) Smoothed hexahedral mesh
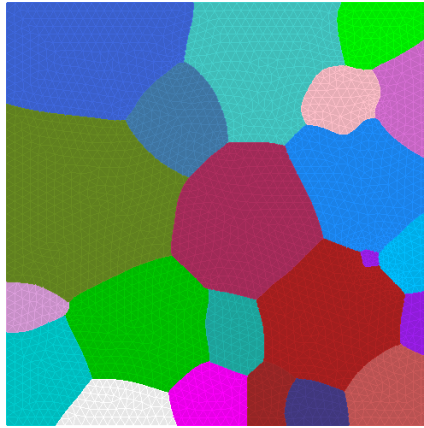
(c) Smoothed tetrahedral mesh

Fig. 9 Mesh types created for a synthetic microstructure

Nine representative FE meshes of the B_4C-TiB_2 ceramic composite are shown in Fig. 10. These meshes represent smoothed grains with hexahedral elements. Each SVE has an edge length of 25 μm. Meshes are used in fracture simulations with the phase field method: the former are discussed in Section 4, following presentation of the phase field theory and its 3-D numerical implementation next in Section 3.

The volumes for all of the grains in our final SVE meshes were extracted using Sculpt. The equivalent diameters were calculated and plotted as CDFs for each of the SVEs (Fig. 11). The black dashed line corresponds to the equivalent diameter fit for all grains in the experimental EBSD (Section 2.2). As previously mentioned, small grains less than 2 micron in diameter are not included in the experimental fit or synthetic generation. Using the KS statistic procedures mentioned before, the statistic for difference between the EBSD grains and the synthetic microstructures generated ranged between 0.05 and 0.147, and the p-values ranged between 0.024 and 0.214.
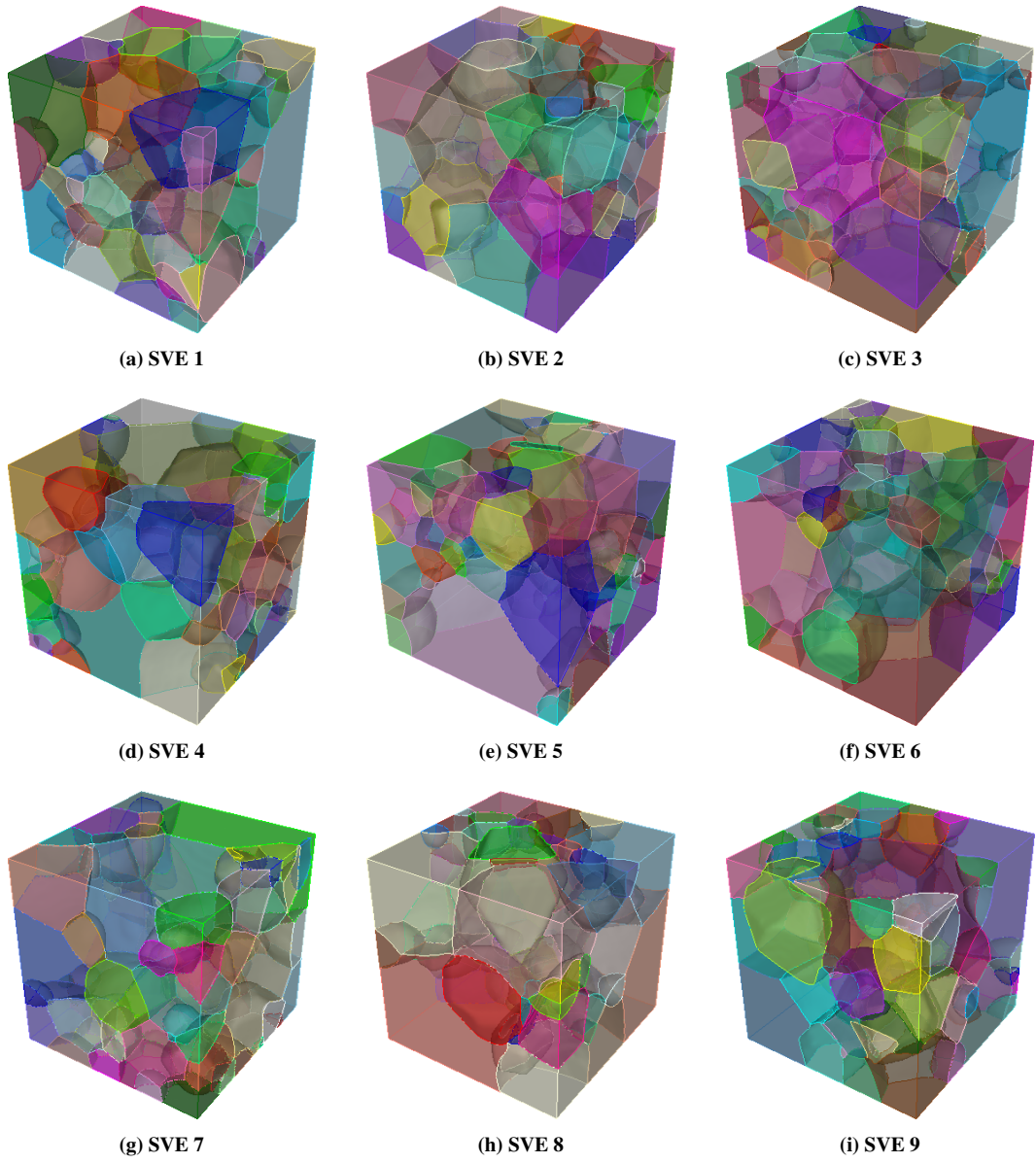
(a) SVE 1

(b) SVE 2

(c) SVE 3

(d) SVE 4

(e) SVE 5

(f) SVE 6

(g) SVE 7

(h) SVE 8

(i) SVE 9

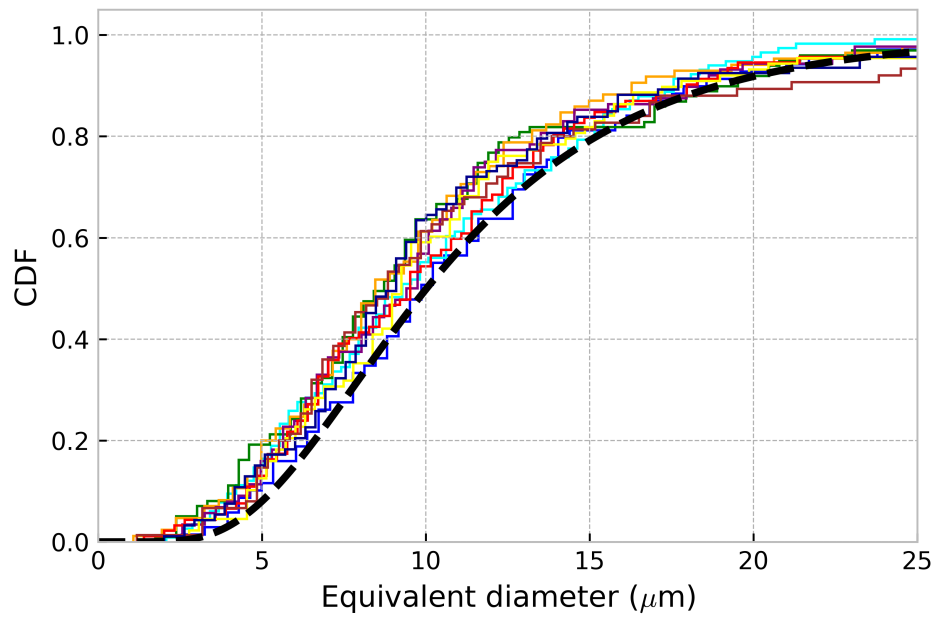**Fig. 10 Nine synthetic volume element realizations (SVEs)**

Fig. 11 CDF for all grains in EBSD and smoothed SVEs

3. Phase Field Methods

3.1 Theory

Presentations of the phase field theory, potentially including nonlinear elasticity and dissipative kinetic effects as well as residual stress fields, are given in prior work.[45,47,51] An abbreviated presentation is given here, focused on physics addressed in problems solved in Section 4 and in two of our most recent articles.[52,53] Plastic slip, deformation twinning, phase transitions, temperature changes, thermal expansion, and residual stresses described in prior theoretical and computational work[45,47] are not included here. On the other hand, the present theory does include anisotropic elasticity, anisotropic fracture energy, and dissipative fracture kinetics. The latter features a potentially state-dependent, finite crack viscosity enabling rate dependence than can vary among different local stress states. Cartesian coordinates are implied in the theoretical presentation; more general curvilinear coordinates are used elsewhere.[45,46] Isothermal conditions are invoked in thermodynamics, and inertial forces associated with stress wave propagation are absent.

Denote by $\boldsymbol{u} = \boldsymbol{u}(\boldsymbol{X}, t)$ the displacement vector, with $\boldsymbol{X}$ the reference position of a material particle and t time. Denote by ∇A the gradient of differentiable function A with respect to $\boldsymbol{X}$, and by $\dot{A}$ the material time derivative of A. Denote by $\xi(\boldsymbol{X}, t) \in [0, 1]$ the order parameter, where $\xi(\boldsymbol{X}) \to 1$ as the material element at $\boldsymbol{X}$ fractures.

The free energy density for a homogeneous material region with properties not explicitly dependent on $\boldsymbol{X}$ is

$$\psi = \psi(\nabla \boldsymbol{u}, \xi, \nabla \xi) = W(\boldsymbol{e}(\nabla \boldsymbol{u}), \xi) + f(\xi, \nabla \xi). \tag{11}$$

The strain energy density is W, the phase energy is f, and $\boldsymbol{e}$ is the symmetric strain tensor to be defined explicitly later.

Denote by Γ the surface energy per unit area, l the regularization length, $\boldsymbol{m}$ a unit normal vector to a preferred fracture plane, and $\omega \geq 0$ a dimensionless parameter (e.g., $\omega = 0$ for isotropic fracture surface energy represented by f). The phase energy is

$$f = (\Gamma/l)[\xi^2 + l^2\{\boldsymbol{1} + \omega \cdot (\boldsymbol{1} - \boldsymbol{m} \otimes \boldsymbol{m})\} : \{\nabla \xi \otimes \nabla \xi\}]. \tag{12}$$

Denote by C the fourth-order tangent elastic modulus tensor and $\zeta \in [0, 1]$ a residual stiffness constant used for numerical stability.[26,27] Then the strain energy density and tangent elastic coefficients are as follows:

$$W(e, \xi) = \tfrac{1}{2}e : C(e, \xi) : e - \tfrac{1}{6}\mathbb{B} \cdot (\mathrm{tr}e)^3 \mathrm{H}(-\mathrm{tr}e), \tag{13}$$

$$C_{IJKL} \begin{cases} = (C_0)_{IJKL}[\zeta + (1 - \zeta)(1 - \xi)^2] & [\text{if } J(e) > 1] \\ = (C_0)_{IJKL}[\zeta + (1 - \zeta)(1 - \xi)^2] & [\text{if } J(e) \leq 1] \\ \quad + B_0 \delta_{IJ}\delta_{KL}[1 - \zeta - (1 - \zeta)(1 - \xi)^2]. \end{cases} \tag{14}$$

The elastic moduli and bulk modulus of the pristine solid are C_0 and B_0. The tangent bulk modulus is degraded in tension ($J > 1$) but retained otherwise.[25] The unit right-continuous Heaviside function is $\mathrm{H}(\cdot)$, where $\mathrm{H}(A) = 1$ for $A \geq 0$ and $\mathrm{H}(A) = 0$ for $A < 0$.

The strain tensor e, volume ratio J, and higher-order bulk compression constant $\mathbb{B}$ are defined differently for nonlinear and linear elasticity. For nonlinear elasticity, numerous options exist for a finite strain measure e.[1,3,5–9] In the present discussion, and as implemented in 1-D problems with analytical solutions,[53] a logarithmic material strain[6] is used here for demonstration:

$$e = \tfrac{1}{2}\ln(F^{\mathrm{T}}F), \quad J = \det F = \exp[\mathrm{tr}(e)], \quad F = \mathbf{1} + \nabla u. \tag{15}$$

The two-point deformation gradient tensor is $F(X, t)$, and J the Jacobian determinant. In this case, $\mathbb{B} = B_0 \cdot (B_0' - 2)$, where B_0' is the initial pressure derivative of the bulk modulus.[6,7] The symmetric Cauchy stress is S, and $P = \partial\psi/\partial\nabla u$ is the first Piola-Kirchhoff stress:

$$S = J^{-1}PF^{\mathrm{T}} = J^{-1}\{(\partial W/\partial e) : (\partial e/\partial F)\}F^{\mathrm{T}} = S^{\mathrm{T}}. \tag{16}$$

The derivative of the logarithmic strain with respect to the deformation gradient F is non-trivial; derivations of necessary terms are given elsewhere.[6,45,72,73]

For linear elasticity, $\mathbb{B} = B_0 \cdot (2B_0' - 1)$, as shown effective in prior analysis of hydrostatic and uniaxial strain compression of crystalline solids.[45] The infinitesimal strain measure is denoted by e for linear elastic constitutive behavior, and the stress

tensors S and P are identical from geometric linearization (i.e., $||\nabla u|| \ll 1$):

$$e = \tfrac{1}{2}[\nabla u + (\nabla u)^{\mathrm{T}}], \quad J = 1 + \nabla \cdot u = 1 + \mathrm{tr} e, \tag{17}$$

$$S = \partial W / \partial e = S^{\mathrm{T}} = P = \partial \psi / \partial \nabla u. \tag{18}$$

The local governing equations can be derived from variational methods[27,31] or a micro-force balance in conjunction with the first and second laws of thermodynamics.[45,74] The essential results are combined with the form of free energy density in Eq. 11, which is written in a general way to encompass both nonlinear and geometrically linear theory.

The governing equations so derived are the linear momentum balance (with null acceleration), natural boundary conditions (with n a unit outward normal to the body), and a kinetic law for the rate of ξ:

$$\nabla \cdot P = \nabla \cdot (\partial W / \partial \nabla u) = 0, \qquad [(\nabla \cdot P)_k = \partial P_{kJ} / \partial X_J]; \tag{19}$$

$$t = P \cdot n, \qquad s = \partial f / \partial \nabla \xi \cdot n; \tag{20}$$

$$\beta \dot{\xi} = -\delta \psi / \delta \xi = -[\partial \psi / \partial \xi - \nabla \cdot (\partial f / \partial \nabla \xi)]. \tag{21}$$

On the boundary of the domain, the mechanical traction t is conjugate to the particle velocity vector $\dot{u}$, and the thermodynamic force s is conjugate to the order parameter rate $\dot{\xi}$.

The viscosity coefficient β is required to be non-negative so that local dissipation $\beta \cdot (\dot{\xi})^2 \geq 0$ unconditionally obeys the second law.[74] Other kinetic equations are possible that satisfy thermodynamic principles,[24,36,41,45] but Eq. 21 (i.e., the time dependent Ginzburg Landau (TDGL) or Allen-Cahn equation) drives the material to a minimum energy state and is the most common prescription.[74,75]

The kinetic coefficient is almost universally assumed a positive *constant* for convenience,[76–79] but thermodynamic derivations[45,74] permit β to be a *function* of local state variables as well as order parameter rate and the velocity gradient:

$$\beta = \beta(\nabla u, \xi, \nabla \xi; \nabla \dot{u}, \dot{\xi}) \geq 0. \tag{22}$$

21

A novel aspect of the model recently theorized and implemented by the authors[53] is the following choice of Eq. 22:

$$\beta(\nabla \boldsymbol{u}, \xi) = \beta_0 \cdot \exp\{a \cdot \langle \Sigma(\nabla \boldsymbol{u}, \xi)\rangle^b\}; \tag{23}$$

$$\Sigma = 3p/\tau, \quad p = -\tfrac{1}{3}\mathrm{tr}\boldsymbol{S}, \quad \tau = \{\tfrac{3}{2}(\boldsymbol{S}+p\mathbf{1}):(\boldsymbol{S}+p\mathbf{1})\}^{1/2} \geq 0. \tag{24}$$

Three independent material constants are $\beta_0 \geq 0$, $a \geq 0$, and $b \geq 0$. The Cauchy pressure is p, and τ is the von Mises deviatoric (shear) stress. Angled brackets parse positive values via $\langle(\cdot)\rangle = \tfrac{1}{2}[(\cdot) + |(\cdot)|]$, and Σ measures triaxiality, positive for compression.

For tensile or neutral loading, $\Sigma \leq 0 \rightarrow \beta = \beta_0$ in compression $\Sigma > 0$, so viscous fracture resistance increases in Eq. 21: $\beta \geq \beta_0$, with $\beta \rightarrow \infty$ as $\tau \rightarrow 0$ for pure hydrostatic compression when $p = \tau = 0$, $\Sigma = 0$ is used. The particular three-parameter function in Eq. 23 has been physically validated by its capability to match the observed pressure-dependent fracture strength of a brittle material,[53] namely polycrystalline B_4C. To avoid confusion on the notation, it is remarked that often in the porous metals literature,[80–82] the quantity $-\Sigma/3 = -p/\tau$, positive in tension, is used for triaxiality.

3.2 Numerical Implementation

Denote by $\boldsymbol{\epsilon}$ an average strain tensor for the material domain of interest Ω_0 represented in FE simulations. Consider boundary conditions on the outer surface of the domain $\partial\Omega_0$ whereby a constant magnitude of macroscopic strain rate, denoted by the scalar $\dot{\epsilon} > 0$, is applied. In general, $\dot{\epsilon}$ scales the components of the applied strain tensor $\boldsymbol{\epsilon}$, where the choice of components and their signs determine the average stress state (e.g., tensile loading, unconfined compression, confined compression, etc.).

As shown in prior work,[45,52] outcomes of the governing equations of the present phase field model at a given applied strain $\boldsymbol{\epsilon}$, not necessarily equal to any local strain component $e_{IJ}(\boldsymbol{X}, t)$, depend on time and crack viscosity only through the dimensionless product $\tilde{\beta}_0\dot{\epsilon}$, where the normalized viscosity $\tilde{\beta}_0 = \beta_0 \cdot l/\Gamma$ has dimensions of time.

Over the duration of any given initial-boundary-value problem, β_0, l, Γ, $\tilde{\beta}_0$, and $\dot{\epsilon}$ are constants, so time is interchangeable with $\epsilon = \dot{\epsilon}t$ as the load parameter. This results in the linear transformation $\tilde{\beta}\dot{\xi} = \tilde{\beta}\dot{\epsilon}\,\mathrm{d}\xi/\mathrm{d}\epsilon$. In practice,[52] simulations for materials with different kinetic viscosity $\tilde{\beta}_0$ are performed at fixed $\dot{\epsilon}$ while varying $\tilde{\beta}_0$, though the converse approach of varying the applied strain rate while fixing the viscosity prefactor yields the same solutions versus ϵ.

The dimensionless time domain of a given problem is decomposed into numerous steps. For a constant applied loading (strain) rate $\dot{\epsilon}$, the dimensionless time differential is simply identified with the applied strain differential, that is, $\mathrm{d}\epsilon = \dot{\epsilon}\mathrm{d}t$. At each time/strain step, the stress field is obtained that simultaneously satisfies the linear momentum balance and constitutive equations of Section 3.2, with details depending on model specifics regarding anisotropy and nonlinearity. The order parameter field is obtained by implicit integration of the general kinetic law of Eq. 21, which holds for anisotropic or isotropic response.

To enable an implicit FE implementation, the variational formulation of the finite element problem for the coupled mechanical and phase-field equations is derived from the mechanical equilibrium equation in Eq. 19 and the phase-field kinetic evolution equation in Eq. 21. The latter order parameter evolution equation for $\mathrm{d}\xi$ is discretized in time with the implicit Euler method, which should demonstrate unconditional stability.[83] As a consequence, a system of nonlinear algebraic equations is obtained for the end-of-timestep nodal values of the displacement components and the order parameter. The conjugate gradient method is used to solve this coupled system consistently at each timestep. The present consistent and fully implicit solution scheme implemented here differs from staggered or hybrid implicit-explicit schemes often used for phase field kinetics and momentum conservation.[84,85] Detailed derivations are lengthy and outside the scope of the present report; these are deferred to a more comprehensive future presentation in a venue more focused on numerical methods.

The solution procedure for the quasi-static reduction of the model, obtained in the limit $\tilde{\beta}_0 = 0$, likewise uses the conjugate gradient method to solve the equilibrium equations for the displacement field and the phase field consistently at each applied strain increment.[31,33] Verification of solutions in the limit $\tilde{\beta} = 0$ was confirmed by comparison with a fully quasi-static implementation used in prior works.[25,26]

The average Cauchy stress and average fracture order parameter are

$$\boldsymbol{\sigma} = \frac{1}{\Omega_0} \int_{\Omega_0} \boldsymbol{S} \, d\Omega_0, \qquad \bar{\xi} = \frac{1}{\Omega_0} \int_{\Omega_0} \xi \, d\Omega_0. \tag{25}$$

The component of average stress along the direction of loading is σ_{IJ}; there is but one lone non-vanishing component for uniaxial stress conditions simulated in Section 4. The maximum value of this component σ_{IJ} achieved in any simulation is σ_C, and ϵ_C is the value of $\epsilon = \dot{\epsilon}t$ when that stress level is reached at corresponding time t.

4. Phase Field Simulations

Simulations of fracture under tensile loading are reported. Each SVE is a cube-shaped domain of edge length 25 μm, where representative grain geometries were previously shown in Fig. 10. The total number of grains for the generated SVEs varied between 70 and 117, with an average element size of $0.132 \, \mu$m, which corresponds to approximately 190 elements across the length of the SVE. The phase field theory is that of Section 3, with $a = b = 0$ since strengthening of the material under compressive states (i.e., $\Sigma > 0$) is irrelevant for tensile pressures witnessed in these simulations. Similarly, $\mathbb{B} = 0$ without consequence since volumetric strains are dilatational.

Table 1. Physical parameters for B$_4$C and TiB$_2$[47,52]

Parameter (units)	B$_4$C	TiB$_2$	Description
C_{11} (GPa)	543	660	single crystal elastic constants
C_{12} (GPa)	131	48	
C_{13} (GPa)	64	93	
C_{14} (GPa)	−18	0	
C_{33} (GPa)	535	432	
C_{44} (GPa)	165	260	
Γ (J/m^2)	3.27	4.14	fracture surface energy
l (μm)	0.132	0.132	regularization length
ω (-)	10	100	cleavage anisotropy
$\tilde{\beta}_0 \dot{\epsilon}$ (-)	10^{-4}	10^{-4}	viscosity $\times$ applied strain rate

The physical properties used for single crystals of each of the B$_4$C and TiB$_2$ phases, as tabulated in Table 1, are within ranges of those of other recent works on tensile fracture on these two materials and their ceramic blends.[47,52] Second-order elastic

constants $C_{\alpha\beta}$ correspond to $(C_0)_{IJKL}$ of Eq. 14 and follow Voigt notation, where $\alpha, \beta = 1, 2, \ldots 6$. The number of independent anisotropic elastic constants is five for TiB$_2$ (hexagonal structure) and six for B$_4$C (trigonal structure).

The geometrically linear theory is used in 3-D FE simulations, such that Eqs. 17 and 18 hold. Linear anisotropic elasticity and anisotropic cleavage surface energy are implemented. The residual stiffness factor is set to $\zeta = 0.01$ for stability. Boundary conditions correspond to macroscopic states of uniaxial stress. Taking X_1 as the loading direction, the only non-negligible component of the average stress of Eq. 25 is σ_{11}, and the corresponding applied strain is ϵ_{11}. The dimensionless applied strain rate in the X_1 direction, which affects strength for rate-dependent fracture, is $\tilde{\beta}_0 \dot{\epsilon}$.

In Fig. 12, the stress magnitude at late time is shown for SVE 9 for uniaxial tension applied in the X_1 direction. Completely failed regions are hidden to highlight the sample failure. Stress magnitude concentrations can be seen on the top in red, highlighting the tip of the cracking regions. The plotting of the stress is created element-wise, based on the regularization region of the phase field code, and highlights the voxelized averaging. Decreasing the size of the grid used gets closer visualizations to the smooth grain structures used in the simulations.
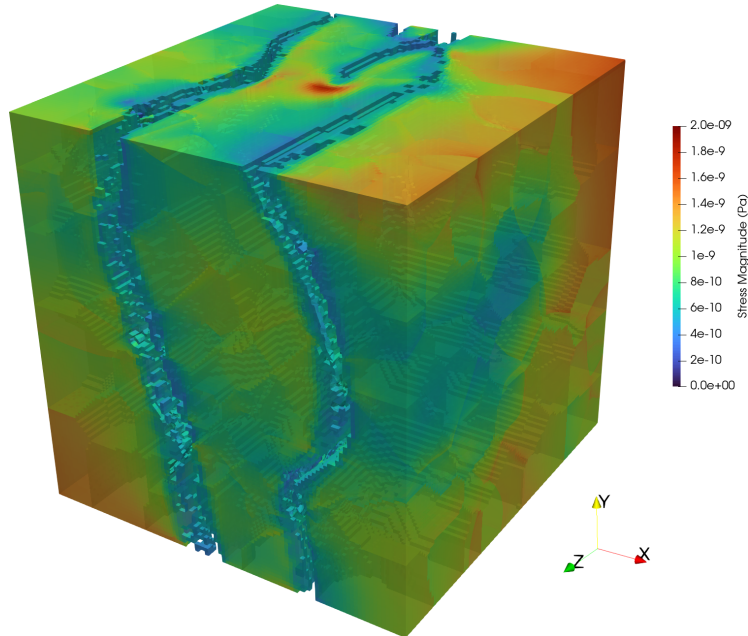

Fig. 12 Tensile failure of SVE 9 colored by stress magnitude

4.1 Grain Geometries

Average stress-strain data are reported for nine microstructure instantiations in Fig. 13. Each separate SVE has unique grain geometries generated based on the material statistics. Uniaxial tension loading was completed in all three cardinal directions. Random orientations are applied to all the grains, but the orientations remained fixed for each SVE when the loading direction was changed. Differences in microstructure lead to different values of peak load σ_C and corresponding average strain ϵ_C among simulations.

All of the individual loading directions are combined into one plot to show the distribution of stress and strain due primarily to grain geometry. In Fig. 14, blue opacity is used to better see the clustering or concentration of stress-strain responses for the nine SVEs. The mean failure stress for 27 simulations with 9 geometry instantiations was 1.736 ± 0.0374 GPa.

Our traditional Weibull modulus analysis of sample failure probability for the uniaxial tension simulations is shown in Fig. 15, following procedures previously reported.[86] In the plots, the x-axis failure stress is normalized by the the median stress. The probability that a sample is safe from failure is related to the failure probability ($P_{safe} = 1 - P_{fail}$). Preliminary analysis indicates that without the incorporation of initial porosity or initial defects to drive material failure, the Weibull modulus $m = 54.42$ appears to be higher (less variable) than expected experimentally. It is similar to the $m = 62.95$ result from the 3-point bend tests of the fine-grain B_4C-TiB_2 in Rubink.[54] Values of m ranging from 4.8 to 35.3 were reported by Wereszczak et al.[87] on hot-pressed B_4C from equibiaxial flexure and Hertzian indentation tests, where the latter spherical indentation results probed much smaller volumes and gave much higher mean stresses, with less variability.
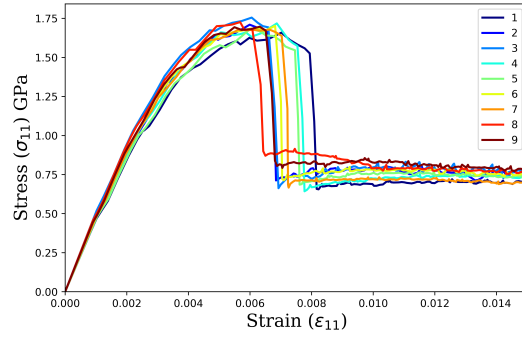
(a) X_1-**direction loading**
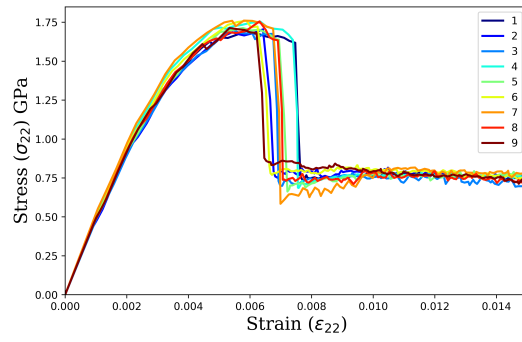
(b) X_2-**direction loading**
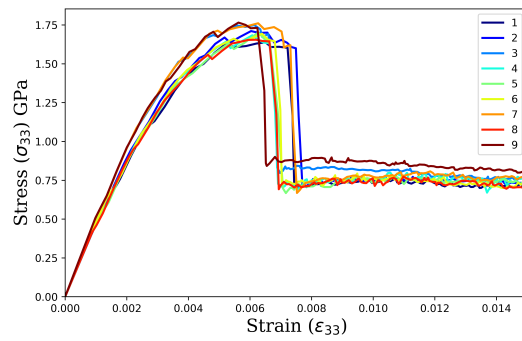
(c) X_3-**direction loading**

Fig. 13 Average stress-strain response for varied geometries in each loading direction
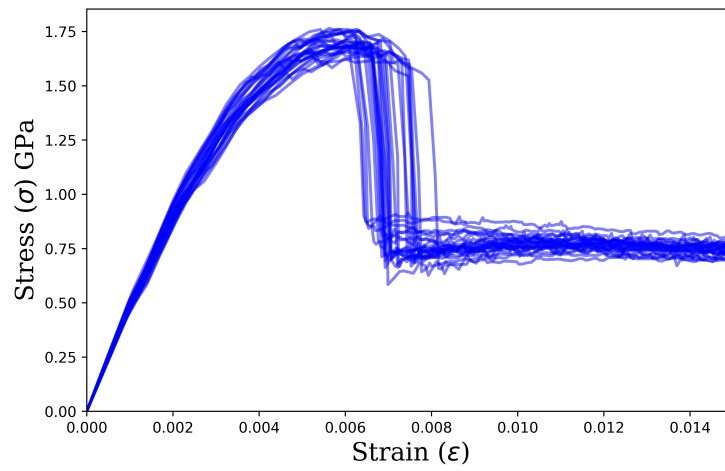
Fig. 14 Combined plot of stress-strain response in all directions for varied geometries
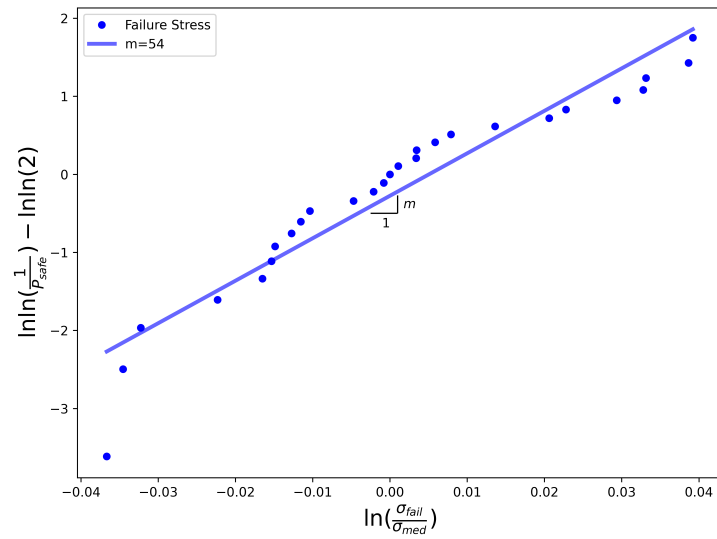

Fig. 15 Weibull plot of normalized peak failure stress for varied geometries
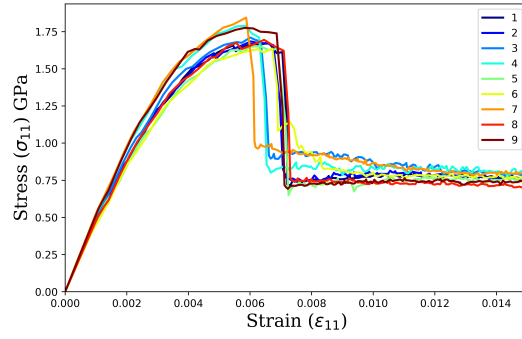
4.2 Grain Orientations

In contrast to changing the realizations and grain geometries in Section 4.1, as shown in the previous stress-strain curves of Figs. 13 and 14, now in Section 4.2 just one SVE was chosen as the grain geometry, with nine different random orientations instantiated using the same SVE. These simulations with nine different orientations and the same microstructure are then repeated with tensile loading in the three cardinal directions.

In Fig. 16, SVE 9 stress-strain responses are shown for loading in the three loading directions, with only the individual grain orientations randomly changing for the different runs. Recall that according to the anisotropic PFM of Section 3, different lattice orientations of the grains with respect to the loading direction will produce different mechanical results arising from anisotropic elastic constants $C_{\alpha\beta}$ and orientations of dominant cleavage planes $\boldsymbol{m}$ as manifested by $\omega > 0$ in Eq. 12.

All of the individual loading directions are combined into one plot to show the distribution of stress and strain, with differences due primarily to grain orientations. In Fig. 17, green opacity is used to better see the clustering or concentration of stress-strain responses for the nine different random lattice orientation distributions for this SVE. The mean failure stress for the 27 simulations with 9 different sets of grain orientations was 1.728 ± 0.0519 GPa, which was more variable than the grain morphology/structure-changed simulations of Section 4.1.

The Weibull modulus analysis for the uniaxial tension simulations in which the geometry stays fixed, and nine different orientation instantiations are used, is shown in Fig. 18. The Weibull modulus $m = 38.09$ appears to be lower (more variable) than the simulations in which the microstructure's geometries were changed with lattice orientations held fixed for each SVE of the same geometry. Of course, the large TiB$_2$ grains in SVE 9 may contribute to the increased variability due to orientation changes.

(a) X_1**-direction loading**
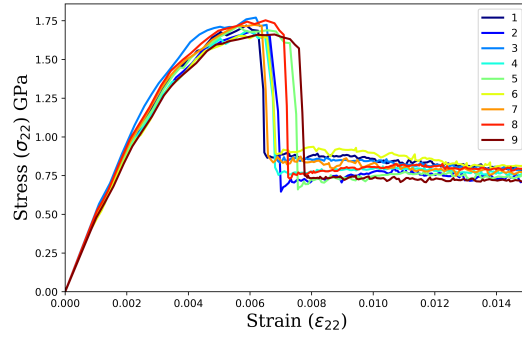
(b) X_2**-direction loading**
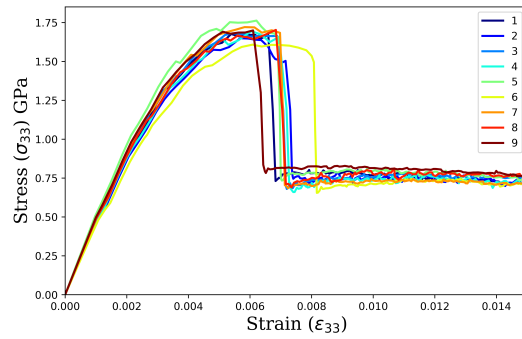
(c) X_3**-direction loading**

Fig. 16 Average stress-strain response for varied orientations in each loading direction
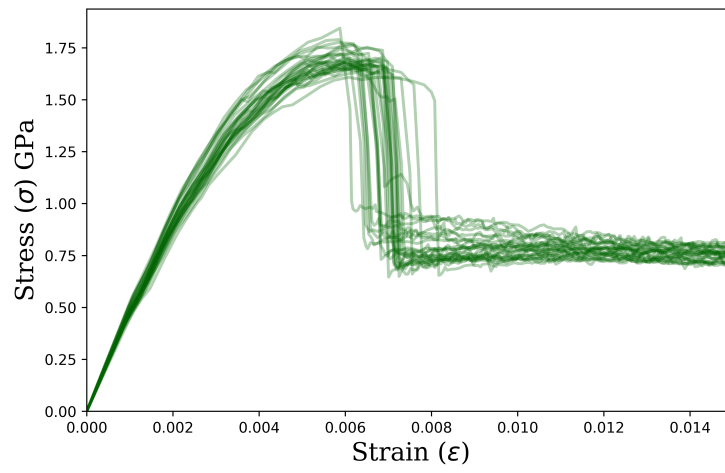
Fig. 17 Combined plot of stress-strain response in all directions for varied orientations

Fig. 18 Weibull plot of normalized peak failure stress for varied orientations

4.3 Size Scaling

As reported in Section 4.2, the representative strengths fluctuate around $\sigma_C = 1736 \pm 37$ MPa, for SVE cross-sectional areas of 25×25 μm^2 and nine SVE microstructures each loaded under tension in one of three cardinal directions. For comparison, the dynamic flexure strength of polycrystalline B_4C produced by SPS was measured experimentally,[54] for a specimen in 3-point b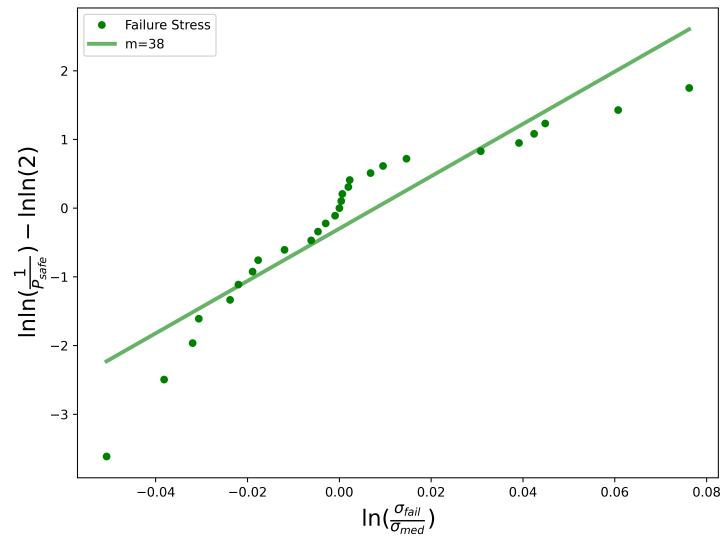ending of cross-sectional area of 3×4 mm^2, to be 434 ± 118 MPa, and the dynamic tensile strength value for an SPS-produced B_4C-TiB_2 composite was likewise measured[54] at 574 ± 29 MPa.

Assuming that the results of the phase field simulations are physically representative, then a Weibull strength-size scaling factor can be estimated from the volume and area scaling relations between different experiments,[88]

$$\frac{\sigma_{C1}}{\sigma_{C2}} = \left(\frac{V_2}{V_1}\right)^{1/m_V}, \tag{26}$$

where m_V is the scaling Weibull modulus, V is the stressed volume of the sample, and subscripts 1 and 2 denote different sized samples. If cross-sectional areas are used instead of volumes, Vs become Ss for areas, and the area scale factor will be denoted m_S. Note that this Wiebull strength-size scale factor for volumes (m_V) or for areas (m_S) is different from the the Weilbull modulus (m) used to report variability in the observed results of experiments and simulations throughout this report.

Taking $\sigma_{C1}/\sigma_{C2} \approx 1736/500 \approx \frac{7}{2}$ (i.e., an approximate average of 500 MPa over static and dynamic strengths for the experimental value σ_{C2} at the larger scale) and $V_2/V_1 \approx S_2/S_1 = 12/6.25 \cdot 10^{-4} = 1.92 \cdot 10^4$ gives a Weibull area scale factor of $m_S \approx \ln 5500 \approx 8.60$. This first estimate assumes stressed volumes are proportional to cross-sectional areas. Taking $\sigma_{C1}/\sigma_{C2} \approx \frac{7}{2}$ and $V_2/V_1 \approx (S_2/S_1)^{3/2} = 2.66 \cdot 10^6$ gives a Weibull volume scale factor of $m_V \approx 13.5$. This second estimate assumes stressed volumes are proportional to cross-sectional areas$^{3/2}$.

Fig. 19 uses the strength size scaling plotting approach from ASTM-C1683.[89] The B_4C-TiB_2 results are shown in blue with B_4C tension experimental results shown in purple. The plots use effective volumes (V_E) instead of areas and the characteristic (mean) failure strengths (σ_C) for experiments. The Rubink 3-point bend tests[54] along with the SVE tension simulations for B_4C-TiB_2 gives $m_V = 15.69$.
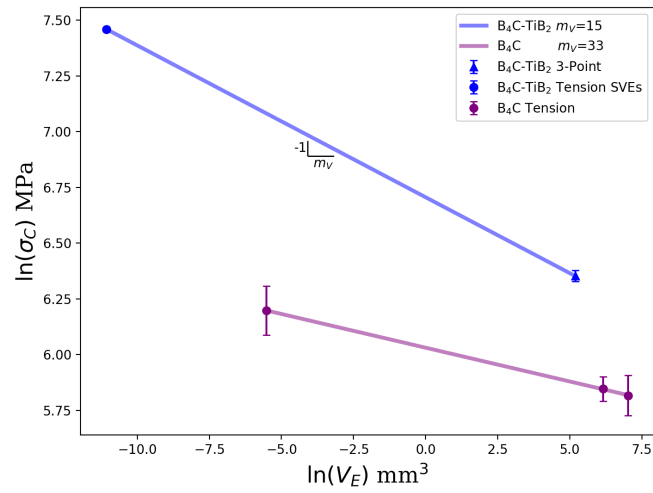
Fig. 19 Weibull strength size scaling for B$_4$C (purple) and B$_4$C-TiB$_2$ (blue)

The ability to determine effective volumes and characteristic strengths for mixed stress state loading like bending remains an area of interest to the authors. Ideally, size scaling determinations are made using tension of vastly different sample sizes to capture consistent sample size failure strengths.

For comparison, the volume scaling for B_4C using only tension tests from Swab[90] and Magagnosc[91] gives $m_V = 33.04$. When porosity and defects are included in the simulations, the predicted mean tensile strength at the smaller size of the SVEs will be reduced, becoming closer to the experimental mean. This in turn will lead to a higher value of m_V computed by the present approach that uses combined experimental and simulation data.

Furthermore, because the present PFM simulations invoke mildly dynamic loading (i.e., $\tilde{\beta}\dot{\epsilon} = 10^{-4} > 0$ in Table 1), a mean static peak stress from simulations[52] would be slightly lower than the obtained value of 1736 MPa with identical prescriptions of the other geometric and material parameters. The ratio σ_{C1}/σ_{C2} would in turn be lower in the true static limit. This would lead to a higher value of m_V computed by the size scaling technique just invoked, that is, a value of m_V closer to the B_4C experimental value of 33 for this material system.

5. Conclusions

A 7-step experimental-computational workflow, spanning from 1) materials characterization to 2) statistical representations to 3) synthetic microstructure generation to 4) conformal FE meshing to 5) PFM implementation and parameterization to 6) phase field simulations of elasticity and fracture mechanics to 7) comparison of mechanics simulations and experiment, has been demonstrated. Methods for computer rendering of microstructures of polycrystalline solids have been described in detail, with a focus on application to B_4C and TiB_2-based ceramics. These procedures make prominent use of the DREAM3D, Cubit , and Sculpt software packages.

Prior work on the PFM for simulating fracture and other structural changes in solids has been briefly reviewed. A novel phase field theory for transient fracture mechanics, and its implicit numerical implementation in 3-D FE software written at ARL, have been summarized.

Results from demonstrative simulations of fracture under dynamic tensile loading have been presented. Different failure strengths have been observed among different grain geometric instantiations of microstructure. Different failure strengths have also been determined for the same microstructure and different relative loading and lattice orientations. The failure strength distributions based on the variation of granular lattice orientations were more variable than the strength variations due primarily to geometry changes. Weibull moduli computed from purely simulated peak stresses for constant-size SVEs quantify this trend, but these values of the Weibull moduli appear larger than might be expected based on experimental findings for other ceramics.

The larger tensile strengths of smaller samples probed in simulations, compared to smaller strengths and larger sample sizes measured experimentally, have been alternatively examined using Weibull size scaling. Values of the resulting calculated (scaled) Weibull modulus are physically reasonable when compared to Weibull modulus values fitted to purely experimental, quasi-static data for polycrystalline material volumes of present relevance for B_4C and B_4C-23 vol.%TiB_2.

The current results of the phase field simulations suggest that the incorporation of defects and porosity along with larger SVEs may be appropriate. Future simulations with a larger number of orientation instantiations and fewer microstructures may also be prudent. Suggestions for improvement to the geometry based on additional characterization efforts may be considered in future simulations. Specifically, the TiB_2 grains may be more disc-shaped and less spherical than described in the current simulations. These geometric and simulation changes, along with more realistic texture bias for the TiB_2 grains, may improve the realism of the phase field simulations. The incorporation of the phase field results and statistics for upscaling into macroscale ceramic models will be discussed in upcoming report(s).

6. References

1. Thurston R. Waves in solids. In: Handbuch der physik; Vol. 4; Springer; 1974. p. 109–308.

2. Teodosiu C. Elastic models of crystal defects. Springer; 1982.

3. Clayton J. Nonlinear mechanics of crystals. Springer; 2011.

4. Srinivasa A. On the use of the upper triangular (or QR) decomposition for developing constitutive equations for Green-elastic materials. International Journal of Engineering Science. 2012;60:1–12.

5. Clayton J. Nonlinear Eulerian thermoelasticity for anisotropic crystals. Journal of the Mechanics and Physics of Solids. 2013;61:1983–2014.

6. Clayton J. Analysis of shock compression of strong single crystals with logarithmic thermoelastic-plastic theory. International Journal of Engineering Science. 2014;79:1–20.

7. Clayton J. Nonlinear elastic and inelastic models for shock compression of crystalline solids. Springer; 2019.

8. Clayton J, Freed A. A constitutive framework for finite viscoelasticity and damage based on the Gram-Schmidt decomposition. Acta Mechanica. 2020;231:3319–3362.

9. Wallace D. Thermodynamics of crystals. John Wiley and Sons; 1972.

10. Hill R. The mathematical theory of plasticity. Clarendon Press; 1950.

11. Asaro R. Crystal plasticity. Journal of Applied Mechanics. 1983;50:921–934.

12. Clayton J. A continuum description of nonlinear elasticity, slip and twinning, with application to sapphire. Proceedings of the Royal Society (London) A. 2009;465:307–334.

13. Johnson G, Cook W. A constitutive model and data for materials subjected to large strains, high strain rates, and high temperatures. In: Proceedings of the 7th International Symposium on Ballistics; p. 541–547.

14. Krajcinovic D. Damage mechanics. Elsevier; 1996.

15. Lloyd J, Field D, Limmer K. A four parameter hardening model for TWIP and TRIP steels. Materials & Design. 2020;194:108878.

16. Lloyd J, Field D, Magagnosc D, Limmer K, Turnage S, Williams C, Clayton J. Manipulating shock waves with metallurgy. Acta Materialia. 2022;234:118042.

17. Xu XP, Needleman A. Void nucleation by inclusion debonding in a crystal matrix. Modelling and Simulation in Materials Science and Engineering. 1993;1:111–132.

18. Clayton J, McDowell D. Homogenized finite elastoplasticity and damage: theory and computations. Mechanics of Materials. 2004;36:799–824.

19. Clayton J. Dynamic plasticity and fracture in high density polycrystals: constitutive modeling and numerical simulation. Journal of the Mechanics and Physics of Solids. 2005;53:261–301.

20. Mota A, Knap J, Ortiz M. Three-dimensional fracture and fragmentation of artificial kidney stones. In: Journal of physics: Conference series; Vol. 46; IOP Publishing; 2006. p. 041.

21. Leavy R, Clayton J, Strack O, Brannon R, Strassburger E. Edge on impact simulations and experiments. Procedia Engineering. 2013;58:445–452.

22. Leavy R, Guilkey J, Phung B, Spear A, Brannon R. A convected-particle tetrahedron interpolation technique in the material-point method for the mesoscale modeling of ceramics. Computational Mechanics. 2019;64:563–583.

23. Bourdin B, Francfort G, Marigo JJ. Numerical experiments in revisited brittle fracture. Journal of the Mechanics and Physics of Solids. 2000;48:797–826.

24. Miehe C, Schaenzel LM, Ulmer H. Phase field modeling of fracture in multiphysics problems. Part I. Balance of crack surface and failure criteria for brittle crack propagation in thermo-elastic solids. Computer Methods in Applied Mechanics and Engineering. 2015;294:449–485.

25. Clayton J, Knap J. A geometrically nonlinear phase field theory of brittle fracture. International Journal of Fracture. 2014;189:139–148.

26. Clayton J, Knap J. Phase field modeling of directional fracture in anisotropic polycrystals. Computational Materials Science. 2015;98:158–169.

27. Clayton J, Knap J. Phase field modeling of coupled fracture and twinning in single crystals and polycrystals. Computer Methods in Applied Mechanics and Engineering. 2016;312:447–467.

28. Clayton J, Knap J. Continuum modeling of twinning, amorphization, and fracture: theory and numerical simulations. Continuum Mechanics and Thermodynamics. 2018;30:421–455.

29. Clayton J, Leavy R, Knap J. Phase field modeling of heterogeneous microcrystalline ceramics. International Journal of Solids and Structures. 2019;166:183–196.

30. Clayton J, Rubink W, Ageh V, Choudhuri D, Chen R, Du J, Scharf T. Deformation and failure mechanics of boron carbide-titanium diboride composites at multiple scales. JOM. 2019;71:2567–2575.

31. Clayton JD, Knap J. A phase field model of deformation twinning: nonlinear theory and numerical simulations. Physica D: Nonlinear Phenomena. 2011;240:841–858.

32. Clayton J, Knap J. Phase field modeling of twinning in indentation of transparent single crystals. Modelling and Simulation in Materials Science and Engineering. 2011;19:085005.

33. Knap J, Clayton J. A computational framework for phase-field modeling. Army Research Laboratory (US); 2010. Report No.: ARL-MR-0760.

34. Levitas V, Levin V, Zingerman K, Freiman E. Displacive phase transitions at large strains: phase-field theory and simulations. Physical Review Letters. 2009;103:025702.

35. Kondo R, Tadano Y, Shizawa K. A phase-field model of twinning and detwinning coupled with dislocation-based crystal plasticity for HCP metals. Computational Materials Science. 2014;95:672–683.

36. Miehe C, Hofacker M, Schanzel L, Aldakheel F. Phase field modeling of fracture in multi-physics problems. Part II. Coupled brittle-to-ductile failure crite-

ria and crack propagation in thermo-elastic-plastic solids. Computer Methods in Applied Mechanics and Engineering. 2015;294:486–522.

37. Choo J, Sun W. Coupled phase-field and plasticity modeling of geological materials: from brittle fracture to ductile flow. Computer Methods in Applied Mechanics and Engineering. 2018;330:1–32.

38. Clayton J. Finsler-geometric continuum mechanics. Army Research Laboratory (US); 2016. Report No.: ARL-TR-7694.

39. Clayton J. Finsler geometry of nonlinear elastic solids with internal structure. Journal of Geometry and Physics. 2017;112:118–146.

40. Clayton J. Generalized Finsler geometric continuum physics with applications in fracture and phase transformations. Zeitschrift fur Angewandte Mathematik und Physik (ZAMP). 2017;68:9.

41. Miehe C, Teichtmeister S, Aldakheel F. Phase-field modelling of ductile fracture: a variational gradient-extended plasticity-damage theory and its micromorphic regularization. Philosophical Transactions of the Royal Society A. 2016;374:20150170.

42. Clayton J. Finsler differential geometry in continuum mechanics: fundamental concepts, history, and renewed application to ferromagnetic solids. Mathematics and Mechanics of Solids. 2022;27:910–949.

43. Clayton J, Knap J. Geometric micromechanical modeling of structure changes, fracture, and grain boundary layers in polycrystals. Journal of Micromechanics and Molecular Physics. 2018;3:1840001.

44. Clayton J. Computational modeling of dual-phase ceramics with Finsler-geometric phase field mechanics. Computer Modeling in Engineering and Sciences (CMES). 2019;120:333–350.

45. Clayton J. Nonlinear thermodynamic phase field theory with application to fracture and dynamic inelastic phenomena in ceramic polycrystals. Journal of the Mechanics and Physics of Solids. 2021;157:104633.

46. Clayton J. Thermodynamic phase field models for fracture and inelasticity. DEVCOM Army Research Laboratory; 2021. Report No.: ARL-TR-9320.

47. Clayton J, Leavy R, Knap J. Phase field mechanics of residually stressed ceramic composites. Philosophical Magazine. 2022;102:1891–1944.

48. Clayton J, Williams C. Modelling the anomalous shock response of titanium diboride. Proceedings of the Royal Society of London A. 2022;478:20220253.

49. Clayton J, Guziewski M, Ligda J, Leavy R, Knap J. A multi-scale approach for phase field modeling of ultra-hard ceramic composites. Materials. 2021;14:1408.

50. Clayton J, Zorn J, Leavy R, Guziewski M, Knap J. Phase field modeling of diamond-silicon carbide ceramic composites with tertiary grain boundary phases. International Journal of Fracture. 2022;237:101–138.

51. Clayton J. Modeling deformation and fracture of boron-based ceramics with nonuniform grain and phase boundaries and thermal-residual stress. Solids. 2022;3:643–664.

52. Clayton J, Knap J, Leavy R. On rate dependence and anisotropy in phase field modeling of polycrystalline fracture. Mechanics of Materials. 2023;180:104606.

53. Clayton J, Leavy R, Knap J. Phase field theory for pressure-dependent strength in brittle solids with dissipative kinetics. Mechanics Research Communications. 2023;129:104097.

54. Rubink W, Ageh V, Lide H, Ley N, Young M, Casem D, Faierson E, Scharf T. Spark plasma sintering of B_4C and B_4C-TiB_2 composites: deformation and failure mechanisms under quasistatic and dynamic loading. Journal of the European Ceramic Society. 2021;41:3321–3332.

55. Schindelin J, Arganda-Carreras I, Frise E, Kaynig V, Longair M, Pietzsch T, Preibisch S, Rueden C, Saalfeld S, Schmid B. Fiji: an open-source platform for biological-image analysis. Nature Methods. 2012;9:676–682.

56. Kluyver T et al. Jupyter notebooks-a publishing format for reproducible computational workflows. In: Elpub; p. 87–90.

57. Leavy R. Synthetic microstructure generation (unpublished). DEVCOM Army Research Laboratory; 2020.

58. Kolmogorov A. Sulla determinazione empirica di una lgge di distribuzione. Institute of Italian Actuaries. 1933;4:83–91.

59. Tang W, Ang A. Probability concepts in engineering: Emphasis on applications to civil & environmental engineering. Wiley; 2007.

60. Bishop J, Strack O. A statistical method for verifying mesh convergence in Monte Carlo simulations with application to fragmentation. International Journal for Numerical Methods in Engineering. 2011;88:279–306.

61. Brannon R, Jensen K, Nayak D. Hypervariate constitutive modeling illustrated via aleatory uncertainty in a foundation model. Journal of the European Ceramic Society. 2018;38:2971–2987; Cermodel 2017: Modelling and Simulation Meet Innovation in Ceramics Technology.

62. Groeber M, Jackson M. DREAM.3D: A digital representation environment for the analysis of microstructure in 3D. Integrating Materials and Manufacturing Innovation. 2014;3:56–72.

63. Spear A, Li S, Lind J, Suter R, Ingraffea A. Three-dimensional characterization of microstructurally small fatigue-crack evolution using quantitative fractography combined with post-mortem X-ray tomography and high-energy X-ray diffraction microscopy. Acta Materialia. 2014;76:413–424.

64. Rollett A, Lee S, Campman R, Rohrer G. Three-dimensional characterization of microstructure by electron back-scatter diffraction. Annual Review of Material Research. 2007;37:627–658.

65. Groeber M, Ghosh S, Uchic M, Dimiduk D. A framework for automated analysis and simulation of 3D polycrystalline microstructures. Acta Materialia. 2008;56:1257-1273.

66. Hibbitt H, Karlsson B, Sorensen E. ABAQUS standard user's manual. HKS; 2001.

67. Blacker T, Bohnhoff W, Edwards T. CUBIT mesh generation environment. Volume 1: Users manual. Sandia National Laboratories; 1994.

68. Owen S, Shelton T. Evaluation of grid-based hex meshes for solid mechanics. Engineering with Computers. 2015;31:529–543.

69. Lim H, Abdeljawad F, Owen S, Hanks B, Foulk J, Battaile C. Incorporating physically-based microstructures in materials modeling: Bridging phase field and crystal plasticity frameworks. Modelling and Simulation in Materials Science and Engineering. 2016;24:045016.

70. Schoof L, Yarberry V. EXODUS II: a finite element data model. Sandia National Laboratories; 1994.

71. Maddali S, Ta'asan S, Suter R. Topology-faithful nonparametric estimation and tracking of bulk interface networks. Computational Materials Science. 2016;125:328–340.

72. Miehe C, Lambrecht M. Algorithms for computation of stresses and elasticity moduli in terms of Seth-Hill's family of generalized strain tensors. Communications in Numerical Methods in Engineering. 2001;17:337–353.

73. Jog C. The explicit determination of the logarithm of a tensor and its derivative. Journal of Elasticity. 2008;93:141–148.

74. Gurtin M. Generalized Ginzburg-Landau and Cahn-Hilliard equations based on a microforce balance. Physica D. 1996;92:178–192.

75. Allen S, Cahn J. A microscopic theory for antiphase boundary motion and its application to antiphase domain coarsening. Acta Metallurgica. 1979;27:1085–1095.

76. Jin Y, Wang Y, Khachaturyan A. Three-dimensional phase field microelasticity theory and modeling of multiple cracks and voids. Applied Physics Letters. 2001;79:3071–3073.

77. Karma A, Kessler D, Levine H. Phase-field model of mode III dynamic fracture. Physical Review Letters. 2001;87:045501.

78. Miehe C, Welschinger F, Hofacker M. Thermodynamically consistent phase-field models of fracture: variational principles and multi-field FE implementations. International Journal for Numerical Methods in Engineering. 2010;83:1273–1311.

79. Amirian B, Jafarzadeh H, Abali B, Reali A, Hogan J. Thermodynamically-consistent derivation and computation of twinning and fracture in brittle mate-

rials by means of phase-field approaches in the finite element method. International Journal of Solids and Structures. 2022;252:111789.

80. Marin E, McDowell D. Associative versus non-associative porous viscoplasticity based on internal state variable concepts. International Journal of Plasticity. 1996;12:629–669.

81. Clayton J, Lloyd J. A dynamic finite-deformation constitutive model for steels undergoing slip, twinning, and phase changes. Journal of Dynamic Behavior of Materials. 2021;7:217–247.

82. Clayton J, Lloyd J. Finite strain continuum theory for phase transformations in ferromagnetic elastic-plastic solids. Continuum Mechanics and Thermodynamics. 2022;34:1579–1620.

83. Hoffman J. Numerical methods for engineers and scientists. McGraw-Hill; 1992.

84. Cho JY, Idesman A, Levitas V, Park T. Finite element simulations of dynamics of multivariant martensitic phase transitions based on Ginzburg-Landau theory. International Journal of Solids and Structures. 2012;49:1973–1992.

85. Agrawal V, Dayal K. Dependence of equilibrium Griffith surface energy on crack speed in phase-field models for fracture coupled to elastodynamics. International Journal of Fracture. 2017;207:243–249.

86. Strack O, Leavy R, Brannon R. Aleatory uncertainty and scale effects in computational damage models for failure and fragmentation. International Journal for Numerical Methods in Engineering. 2015;102:468–495.

87. Wereszczak A, Kirkland T, Strong K, Jadaan O, Thompson G. Size scaling of tensile failure stress in boron carbide. Advances in Applied Ceramics. 2010;109:487–492.

88. Quinn G. Weibull strength scaling for standardized rectangular flexure specimens. Journal of the American Ceramic Society. 2003;86:508–510.

89. ASTM. Standard practice for size scaling of tensile strengths using Weibull statistics for advanced ceramics. Annual Book of ASTM Standards. 2015.

90. Swab JS, Pittari J, Gamble W. Uniaxial tensile strength and fracture analysis of a hot-pressed boron carbide. Journal of the European Ceramic Society. 2019;39(6):1965–1973.

91. Magagnosc D, Tonge A. Microscale tension experiments for parameterizing ceramic failure models. Army Research Laboratory (US); 2020. Report No.: ARL-TR-8913.

List of Symbols, Abbreviations, and Acronyms

TERMS:

ARL	Army Research Laboratory
B_4C	Boron Carbide
CDF	Cumulative Distribution Function
CZFEM	Cohesive Zone Finite Element Method
DEVCOM	US Army Combat Capabilities Development Command
DREAM3D	Digital Representation Environment for the Analysis of Microstructure in 3 Dimensions
EBSD	Electron BackScatter Diffraction
eCDF	estimated Cumulative Distribution Function
FE	Finite Element
HEDM	High Energy Diffraction Microscopy
KS	Kolmogorov-Smirnov
PDF	Probability Density Function
PFM	Phase Field Method
RVE	Representative Volume Element
SEM	Scanning Electron Microscopy
SPS	Spark Plasma Sintering
SVE	Synthetic Volume Element
TiB_2	Titanium Diboride

MATHEMATICAL SYMBOLS:

$\boldsymbol{C}$	tangent elastic modulus tensor
D_N	Kolmogorov-Smirnov discrepancy statistic
$\boldsymbol{e}$	strain tensor

45

f	phase energy density
l	regularization length
J	local volume ratio
m	Weibull modulus
p	probability or pressure
$\boldsymbol{S}$	local Cauchy stress tensor
S_N	sample cumulative frequency
$\boldsymbol{u}$	displacement vector
W	strain energy density
$\boldsymbol{X}$	position vector
β	viscosity for phase field kinetics
$\boldsymbol{\epsilon}$	applied strain tensor
$\dot{\epsilon}$	applied strain rate
Γ	surface energy per unit area
μ	mean
ω	fracture anisotropy measure
Ω_0	polycrystal domain
ψ	free energy density
σ	standard deviation
$\boldsymbol{\sigma}$	average Cauchy stress tensor
σ_C	tensile strength
Σ	stress triaxiality
ξ	order parameter
ζ	residual stiffness
$\mathrm{H}(\cdot)$	Heaviside operator
$\nabla(\cdot)$	gradient operator